

# Phase behavior of a binary mixture of patchy colloids: Effect of particle size and gravity

Cite as: J. Chem. Phys. 155, 044903 (2021); doi: 10.1063/5.0056652

Submitted: 12 May 2021 • Accepted: 7 July 2021 •

Published Online: 26 July 2021



View Online



Export Citation



CrossMark

Rodrigo Braz Teixeira,<sup>1,2,a)</sup> Daniel de las Heras,<sup>3,b)</sup> José Maria Tavares,<sup>2,4,c)</sup> and Margarida M. Telo da Gama<sup>1,2,d)</sup>

## AFFILIATIONS

<sup>1</sup> Departamento de Física, Faculdade de Ciências, Universidade de Lisboa, 1749-016 Lisboa, Portugal

<sup>2</sup> Centro de Física Teórica e Computacional, Universidade de Lisboa, 1749-016 Lisboa, Portugal

<sup>3</sup> Theoretische Physik II, Physikalisches Institut, Universität Bayreuth, D-95440 Bayreuth, Germany

<sup>4</sup> Instituto Superior de Engenharia de Lisboa, ISEL, Avenida Conselheiro Emídio Navarro, 1, 1950-062 Lisboa, Portugal

<sup>a)</sup>[rbrazteixeira@gmail.com](mailto:rbrazteixeira@gmail.com)

<sup>b)</sup>URL: [www.danieldelasheras.com](http://www.danieldelasheras.com)

<sup>c)</sup>Author to whom correspondence should be addressed: [jmtavares@fc.ul.pt](mailto:jmtavares@fc.ul.pt)

<sup>d)</sup>[mmgama@fc.ul.pt](mailto:mmgama@fc.ul.pt)

## ABSTRACT

We study theoretically the effect of size difference and that of gravity in the phase behavior of a binary mixture of patchy particles. The species, 2A and 3B, have two A and three B patches, respectively, and only bonds between patches A and B (AB bonds) are allowed. This model describes colloidal systems where the aggregation of particles (3B) is mediated and controlled by a second species, the linkers (2A) to which they bind strongly. Thermodynamic calculations are performed using Wertheim's perturbation theory with a hard sphere reference term that accounts for the difference in the size of the two species. Percolation lines are determined employing a generalized Flory–Stockmayer theory, and the effects of gravity are included through a local density approximation. The bulk phase diagrams are calculated, and all the stacking sequences generated in the presence of gravity are determined and classified in a stacking diagram. The relative size of the particles can be used to control the phase behavior of the mixture. An increase in the size of particles 3B, relative to the size of the linkers 2A, is found to promote mixing while keeping the percolating structures and, in certain cases, leads to changes in the stacking sequence under gravity.

Published under an exclusive license by AIP Publishing. <https://doi.org/10.1063/5.0056652>

## I. INTRODUCTION

The ability to fabricate colloidal particles with well controlled shapes, size distributions, and interparticle interactions has improved considerably in the last few decades,<sup>1</sup> setting the ground for prolific research. Colloidal particles can form crystals, liquids, and other phases of matter also seen in atomic and molecular systems, making them ideal systems to understand the phase behavior. On the other hand, colloidal systems are a form of matter in their own right with structural and thermodynamic properties not seen at the atomic scale.<sup>2</sup> Patchy colloids (colloidal particles with designed patches on their surfaces through which they can form bonds and self-assemble) are a perfect example. Patchy particles are part of a new generation of colloidal particles that are anisotropic. The strong directional interactions between patchy

particles promote phases with peculiar macroscopic properties. Examples include the formation of liquid states with arbitrarily low density (empty liquids)<sup>3</sup> and network fluids (with pinched phase behavior<sup>4</sup> and lower critical points<sup>5</sup>) that can be seen as equilibrium gels. The quest for experimental realizations of equilibrium gels has led to the exploration of linker-particle aggregation. The bonding of particles is mediated by another component, a bifunctional linker. The particles can be, e.g., patchy colloids,<sup>6,7</sup> patchy nanoparticles,<sup>8,9</sup> and biomolecules<sup>10,11</sup> functionalized such that they can bond strongly to a limited number of linkers. In the experimental systems,<sup>6,7,9,11</sup> the size of the linkers is smaller than that of the components to which they bond. The properties of the linkers (e.g., their size, shape, chemistry, and concentration) control the aggregation process and the thermodynamic properties of the system, while the properties of the particles remain the same.<sup>12</sup>

The linker-particle interactions are often engineered using biological macromolecules, such as complementary DNA strands<sup>7,10</sup> or streptavidin and biotin,<sup>6,11</sup> originating extremely strong bonds.

Here, we study both the bulk phase behavior and the sedimentation-diffusion-equilibrium of a colloidal linker-particle system. We model the system as a binary mixture of patchy particles. The model captures the essence of the linker-particle interaction: strong directionality and strength, limited valence, and species of different sizes. The phase behavior of binary mixtures of patchy particles with the same size has been investigated<sup>13,14</sup> for models where bonds can form between patches of particles of the same or different species. The effect on the bulk phase diagram of the number of patches<sup>13</sup> and that of the relative strength of the different bonds<sup>14</sup> was obtained using a combination of Wertheim's first order perturbation theory and a generalized Flory-Stockmayer approach to percolation. Here, we generalize this theoretical framework to the case of species with different sizes and apply it to a model in which only interspecies bonds can form.

In colloidal experiments, gravitational effects are often unavoidable.<sup>15</sup> These effects are particularly strong in sedimentation-diffusion-equilibrium experiments of colloidal mixtures.<sup>16,17</sup> It is frequent to observe a stacking sequence of several layers of distinct bulk phases at different heights in a cuvette<sup>18-20</sup> as a result of a complex interplay of bulk behavior, sedimentation, and diffusion. However, disentangling the effects of interparticle interactions, which generate the bulk phase diagram, from those of gravity is a complex task.<sup>17</sup> We use a theory of sedimentation for colloidal mixtures<sup>17,21</sup> to obtain all possible stacking sequences of the patchy particle model in the limit of samples of infinite height. The theory relates the bulk phase diagram of the mixture to its phase stacking sequences under gravity through a local density approximation (LDA). The theory has been applied to several colloidal mixtures,<sup>21-23</sup> including patchy particle systems<sup>24,25</sup> in which a rich phase stacking phenomenology was found.

This paper is organized as follows: In Sec. II, the patchy particle model of linker-particle aggregation is introduced, Wertheim's perturbation theory for binary mixtures of spheres with different sizes is presented, and the sedimentation theory that incorporates the effect of gravity is summarized. In Sec. III, the results are described in detail: phase diagrams (including percolating lines) for mixtures with equal and different particle sizes as well as all the possible stacking sequences that can be obtained under gravity. Finally, in Sec. IV, the results are summarized and several conclusions are drawn.

## II. MODEL AND THEORY

The system under study is a binary mixture of patchy colloids. The particles are hard spheres (impenetrable spheres that cannot overlap in space) with diameter  $\sigma_i$ . The species is defined by the size of the particle and the number of patches  $n_\alpha^{(i)}$  of type  $\alpha$  on its surface,  $(\alpha, i) = \{(A, 1), (B, 2)\}$ . The pair potential between particles of species  $i$  (with  $n_\alpha^{(i)}$  patches of type  $\alpha$  on its surface) and particles of species  $j$  (with  $n_\beta^{(j)}$  patches of type  $\beta$  on its surface) is given by a repulsive hard sphere potential  $\phi_{HS}$  plus an attractive interaction

between patches on the two particles,

$$\phi(\vec{r}_{ij}) = \phi_{HS}(r_{ij}) - \epsilon_{ij} \sum_{k_i=1}^{n_A^{(i)}} \sum_{k_j=1}^{n_B^{(j)}} \Psi(\vec{r}_{ij}, \hat{r}_{k_i}, \hat{r}_{k_j}). \quad (1)$$

Here,  $\vec{r}_{ij}$  is the vector joining the center of the two particles,  $r_{ij}$  is the distance between the particles, and the sum runs over all the pairs of patches on the two particles. The interaction between patches  $k_i$  on particle  $i$  and  $k_j$  on particle  $j$  is a square well potential of energy  $\epsilon_{ij}$ . The function  $\Psi$  defines the range and shape of this potential and, in general, depends on  $\vec{r}_{ij}$  and the position of the patches on the surface of the particles (represented by  $\hat{r}_{k_i}$  and  $\hat{r}_{k_j}$ ). As explained in more detail in Ref. 26, there are several possible choices for  $\Psi$  (like the one introduced by Bol<sup>27</sup> and known as the Kern-Frenkel potential<sup>28</sup> or the one used in Ref. 29). The results of the present work, given the level of approximation employed in the theory, are compatible with various choices of  $\Psi$ , provided that they define a range small enough to ensure the single bond per patch condition. The choice of simple discontinuous pair potentials like that of Eq. (1) facilitates the definition of a bond: A bond forms when two patches are closer than the range of the patch attraction, and the energy of the bond is equal to the depth of the square well potential.

The systems that motivated this work<sup>6,7,9-11</sup> are binary mixtures engineered in such a way that (i) one of the species (the linker) is bifunctional and therefore may connect to one or two particles of the other species (the monomers), (ii) each monomer can bond to a restricted number of linkers, and (iii) the only bonds that form are those between different species. Therefore, we consider that (i) particles of species 1 have  $n_A = 2$  patches of type A and diameter  $\sigma_1$  and model the linkers (2A), (ii) particles of species 2 have  $n_B > 2$  patches of type B (for simplicity, we choose  $n_B = 3$ ) and diameter  $\sigma_2$  and model the monomers (3B)—see Fig. 1, and (iii) only interspecies bonding is allowed [i.e.,  $\epsilon_{ij} = \epsilon(1 - \delta_{ij})$  in Eq. (1)], and therefore, the model has only one type of bond (AB, i.e., between patches of type A and patches of type B) and a single energy scale,  $\epsilon$ . In what follows, we denote the composition of the mixture  $x$  by the molar fraction of species 2A:  $x_1 = x$ . Hence, the molar fraction of species 3B is  $x_2 = 1 - x$ .

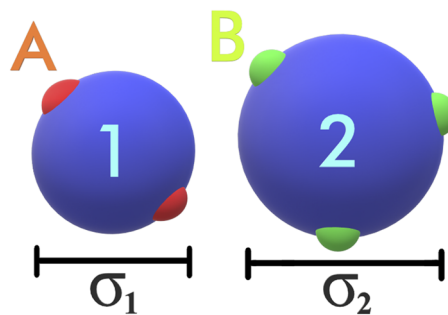


**FIG. 1.** Particle model. Particles of species 1 have diameter  $\sigma_1$  and 2 patches of type A. Particles of species 2 have diameter  $\sigma_2$  and 3 patches of type B. This mixture is referred to as a 2A-3B mixture.

## A. Helmholtz free energy: Wertheim's thermodynamic perturbation theory

Within Wertheim's first order perturbation theory,<sup>30</sup> the Helmholtz free energy per particle,  $f_H$ , is written as a sum of contributions, the unperturbed reference system, containing the excluded volume interactions of the cores and the ideal free energy,  $f_{HS}$ , and a perturbation due to the attractive bonding interactions of the patches,  $f_b$ ,

$$f_H = f_{HS} + f_b. \quad (2)$$

The unperturbed term  $f_{HS}$  is the sum of the ideal gas term that accounts for the kinetic energy (thermal energy) and the excess term that accounts for the excluded volume interactions,  $f_{HS} = f_{id} + f_{ex}$ . For a binary mixture,  $f_{id}$  is given exactly by

$$\beta f_{id} = \ln \rho - 1 + \sum_{i=1,2} x_i \ln(x_i \lambda_i^3), \quad (3)$$

with  $\beta = 1/k_B T$  being the inverse thermal energy ( $k_B$  is the Boltzmann constant and  $T$  is the temperature),  $\rho = N/V$  being the total number density ( $N$  is the total number of particles and  $V$  is the total volume of the system),  $x_i = N_i/N$  being the molar fraction of species  $i$  ( $N_i$  is the number of particles of species  $i$ ), and  $\lambda_i^3$  being the thermal volume of species  $i$ . For the excess part, we use the equation of state proposed by Santos *et al.*,<sup>31</sup> which is based on the Carnahan–Starling equation of state for hard sphere mixtures,<sup>32</sup>

$$\begin{aligned} \beta f_{ex} &= \ln(1-\eta)(-1 + C_2 - 2C_3) \\ &+ \frac{\eta}{1-\eta}(3C_1 + \frac{C_2}{1-\eta} + C_3(\eta-2)), \end{aligned} \quad (4)$$

where  $\eta = \frac{\pi}{6}\rho\langle\sigma^3\rangle$  is the packing fraction of the mixture,  $\langle\sigma^n\rangle = \sum_i x_i \sigma_i^n$  denotes the moments of the diameter distribution, and  $C_i$  are constants given by

$$\begin{aligned} C_1 &= \frac{\langle\sigma\rangle\langle\sigma^2\rangle}{\langle\sigma^3\rangle}, \\ C_2 &= \frac{\langle\sigma^2\rangle^3}{\langle\sigma^3\rangle^2}, \\ C_3 &= \frac{\langle\sigma^2\rangle}{\langle\sigma^3\rangle^2}(\langle\sigma\rangle\langle\sigma^3\rangle - \langle\sigma^2\rangle^2). \end{aligned} \quad (5)$$

The bonding free energy is approximated by Wertheim's first order perturbation theory<sup>33</sup> and comprises two contributions, the bonding energy and an entropic term related to the number of ways of bonding two particles. Denoting by  $X_A$  ( $X_B$ ) the probability that a site of type A (B) on a particle of species 2A (3B) is not bonded, the bonding free energy becomes

$$\beta f_b = xn_A \left[ \ln(X_A) - \frac{X_A}{2} + \frac{1}{2} \right] + (1-x)n_B \left[ \ln(X_B) - \frac{X_B}{2} + \frac{1}{2} \right]. \quad (6)$$

The probabilities ( $X_A, X_B$ ) are related to the total density, molar fractions, and temperature through the laws of mass action (obtained by

treating bond formation as a chemical reaction). These laws form a system of two coupled equations for the fraction of unbonded sites A and B,

$$\begin{aligned} 1 - X_A &= \rho n_B (1-x) X_B X_A \Delta, \\ 1 - X_B &= \rho n_A x X_A X_B \Delta, \end{aligned} \quad (7)$$

which can be solved analytically. Here,  $\Delta$  characterizes the bond between particles of different species. It depends on how the patches are modeled. For patches interacting via a square well with depth  $\epsilon$  [see Eq. (1)], it is given by

$$\Delta = \int_{v_b} g_{HS}^{(12)}(\mathbf{r}) [\exp(\beta\epsilon) - 1] d\mathbf{r}, \quad (8)$$

where  $g_{HS}^{(12)}(\mathbf{r})$  is the radial distribution function of the reference hard sphere fluid for two particles of different species and the integral is calculated over the bonding volume,  $v_b$ , which is constant (all bonds have the same volume). The value of  $v_b$  is set to  $v_b = 0.000\ 332\ 285\sigma_A^3$  as in previous works.<sup>13,14</sup> The radial distribution function  $g_{HS}^{(12)}(\mathbf{r})$  is approximated by its contact value  $A_o(\eta)$ , as obtained from the work of Santos<sup>31</sup> (also based in the Carnahan–Starling contact value<sup>32</sup>),

$$A_o(\eta) = \frac{1}{1-\eta} + \frac{3}{2} \frac{\eta(1-\eta/3)}{(1-\eta)^2} Z + \frac{\eta^2(1-\eta/2)}{(1-\eta)^3} Z^2, \quad (9)$$

where  $Z = 2 \frac{\langle\sigma^2\rangle}{\langle\sigma^3\rangle} \left( \frac{1}{\sigma_1} + \frac{1}{\sigma_2} \right)^{-1}$ . Using  $g_{HS}^{(12)}(\mathbf{r}) = A_o(\eta)$ , Eq. (8) becomes

$$\Delta = v_b [\exp(\beta\epsilon) - 1] A_o(\eta). \quad (10)$$

These approximations are in line with the independent site approximation underlying Wertheim's first order perturbation theory and affect the results quantitatively but are not expected to introduce qualitative changes. A detailed description of Wertheim's theory can be found, e.g., in Refs. 30 and 34. Note that  $v_b$  contains all the dependence of the theory on the specificities (range and form) of the patch–patch square well attraction. Therefore, the theory will give the same results for different choices of  $\Psi$  in Eq. (1), as long as the parameters correspond to the same bonding volume.

The theories adopted to construct the free energy of the mixture have been independently validated by numerical simulations. Agreement between theory and simulations has been found in Ref. 31 for the compressibility factor and for the contact value of  $g(r)$  in binary mixtures of hard spheres of different sizes at several compositions. Likewise, in Ref. 35, the phase behavior of a binary mixture of patchy particles of equal sizes obtained from the theory was shown to be in line with the results of Monte Carlo simulations.

The equilibrium properties of the mixture are determined by minimizing (at a fixed composition  $x$ , osmotic pressure  $p$ , and temperature  $T$ ) the Gibbs free energy per particle,

$$g = \frac{p}{\rho} + f_H, \quad (11)$$

with respect to the total density  $\rho$ , subject to the constraints imposed by the law of mass action, Eq. (7). A standard Newton–Raphson method is used to minimize  $g(x)$ , and the law of mass action is solved analytically. Binodal lines (along which two phases coexist)

are located by a standard common-tangent construction on  $g(x)$ , which is equivalent to solving the equations for the equality of the chemical potentials of both species in the coexisting phases.<sup>36</sup> Mechanical and thermal equilibria are satisfied by fixing both the pressure and the temperature. Critical points are computed by determining the states which satisfy the law of mass action [Eq. (7)] and the spinodal condition,

$$f_{vv}f_{xx} - (f_{xv})^2 = 0, \quad (12)$$

where subscripts denote the partial derivatives, i.e.,  $f_{xv}$  is the second partial derivative of  $f_H$  with respect to the volume per particle  $v = 1/\rho$  and the composition  $x$  at constant temperature. In addition, stability requires the vanishing of the third order derivative in the direction of maximal growth,<sup>37</sup>

$$f_{xxx} - 3f_{xxv}\left(\frac{f_{xv}}{f_{vv}}\right) + 3f_{xvv}\left(\frac{f_{xv}}{f_{vv}}\right)^2 - f_{vvv}\left(\frac{f_{xv}}{f_{vv}}\right)^3 = 0. \quad (13)$$

## B. Flory-Stockmayer random-bond percolation theory for patchy particles

To study percolation, we use the generalization of the Flory-Stockmayer<sup>38,39</sup> random-bond percolation model of Tavares *et al.*<sup>40</sup> Consistent with the assumptions made in Wertheim's theory, closed loops are neglected and the clusters assume a tree-like bonding structure, as illustrated in Fig. 2. Hence, the connections of a cluster can be separated by levels: A random particle is chosen as the level 0; the particles directly connected to this are at level 1, and so-forth. Therefore, the number of bonded sites of type  $\gamma$  on particles of species  $k$  at the level  $i$ ,  $b_{i,\gamma}^{(k)}$ , is related to the number of all types of bonded sites of both species of particles in the previous level,  $b_{i-1,\alpha}^{(j)}$ , through a recursion relation. As explained in detail in Ref. 14, in order to establish if the system has percolated, we express this relation in the matrix form

$$\tilde{b}_i = \tilde{T}^i \tilde{b}_0, \quad (14)$$

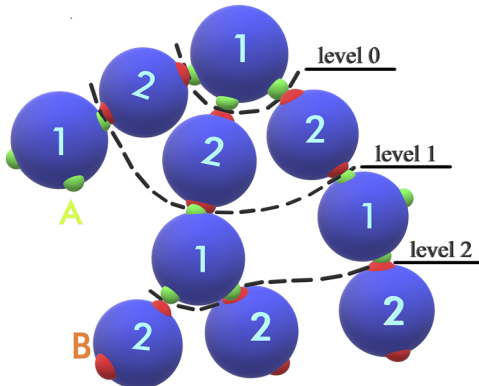


**FIG. 2.** Schematic representation of a tree-like cluster in a binary mixture. After choosing a random particle (top of the figure), the cluster can be represented by levels as shown. At each level, there are  $b_i$  bonded sites. A bond between two bonding sites lowers the energy by  $\epsilon$ . Only bonds of type AB can be formed.

where  $\tilde{b}_i$  is a vector with components  $b_{i,\gamma}^{(k)}$  and  $\tilde{T}$  is a square matrix (the transition matrix) that encodes the connectivity of the cluster. In the mixture under study, the elements of  $\tilde{T}$  are given by

$$\begin{pmatrix} 0 & (1-X_B)(n_B-1) \\ (1-X_A)(n_A-1) & 0 \end{pmatrix}. \quad (15)$$

The matrix  $\tilde{T}$  may be diagonalized or transformed into the Jordan form. In either case, the progressions converge to zero if the largest (absolute value) eigenvalue  $\lambda$  of  $\tilde{T}$  is smaller than one, i.e.,  $|\lambda| < 1$ , since then the number of bonds decreases with increasing level. The percolation threshold is then reduced to determining the states for which the largest absolute value of the eigenvalues of  $\tilde{T}$  is equal to one. That is, the system percolates if the number of bonds increases with increasing level. The eigenvalues of  $\tilde{T}$  are

$$\lambda_{\pm} = \pm \sqrt{(1-X_B)(n_B-1)(1-X_A)(n_A-1)}. \quad (16)$$

The percolation threshold is obtained when the eigenvalue  $\lambda_+$  equals 1. For more details, see Ref. 40.

The average size of the clusters,  $\langle M \rangle$ , which will give insight into the structure of the fluid, is

$$\langle M \rangle = \frac{N}{N_{cl}}, \quad (17)$$

where  $N$  is the total number of particles and  $N_{cl}$  is the number of clusters. Under the no-loop assumption, the number of clusters is  $N_{cl} = N - N_{bonds}$ , where  $N_{bonds}$  is the number of bonds. Hence, every bond reduces the number of clusters by one. One can rewrite Eq. (17) as  $\langle M \rangle = (1 - N_{bonds}/N)^{-1}$ . In this way, the number of bonds per particle may be calculated considering the bonding probabilities,

$$\frac{N_{bonds}}{N} = \frac{n_A x (1-X_A) + n_B (1-x)(1-X_B)}{2}. \quad (18)$$

Plugging Eq. (18) into Eq. (17) gives the expression for the average size of the clusters.

## C. Sedimentation-diffusion-equilibrium

To study the effect of gravity on the phase behavior of the mixture, we use the theory of sedimentation for colloidal mixtures developed by de las Heras and Schmidt.<sup>17</sup> Here, we discuss briefly the main ideas and refer the reader to Refs. 17 and 21 for a detailed description. Gravity is incorporated into the bulk description of the system via a height-dependent local chemical potential for each species defined as

$$\mu_i(z) = \mu_i^b - m_i g z, \quad i = 1, 2, \quad (19)$$

where  $\mu_i^b$  is the bulk chemical potential of species  $i$  (in the absence of gravity),  $m_i$  is the buoyant mass of species  $i$ ,  $g$  is the acceleration due to gravity, and  $z$  is the vertical coordinate. The state of the sample at position  $z$  is therefore approximated by that of an equilibrium system with chemical potentials given by Eq. (19). This local density approximation (LDA) is justified if the correlation lengths in the system are small compared to the gravitational lengths  $\xi_i = k_B T/m_i g$ .

The gravitational length of micrometer-sized colloidal particles typically varies from millimeters to centimeters. Therefore, the LDA is in general a very good approximation.

Eliminating the spatial dependency of the local chemical potentials in Eq. (19) yields

$$\mu_2(\mu_1) = a + s\mu_1, \quad (20)$$

where  $a = \mu_2^b - s\mu_1^b$  and  $s = m_2/m_1$  is the ratio of the buoyant masses. Equation (20) describes a segment of a line in the plane of local chemical potentials, known as the sedimentation path. The representation of the bulk phase diagram in the plane of chemical potentials (at constant temperature) is therefore particularly suited to study sedimentation since the sedimentation paths are simply given by straight lines. In other representations, such as the pressure–composition plane, the sedimentation paths are complex curves,<sup>22</sup> the shape of which depends on the interparticle interactions. The sedimentation path represents how the local chemical potentials vary along the sedimented colloidal mixture. Hence, a sedimentation path that crosses, e.g., a binodal line indicates the presence of an interface in the sedimented sample (see Fig. 3 for an illustration). The sedimentation path is therefore directly related to the observed stacking sequence, i.e., the sequence of different thermodynamic phases observed in sedimentation–diffusion-equilibrium.

We restrict the discussion to samples with very large (infinite) height. This limit is justified in typical sedimentation experiments of micrometer-sized colloidal mixtures since the length of the sedimentation path is typically of several  $k_B T$ , covering a large region of the bulk phase diagram of the mixture. The limit of infinite height sample is very convenient since the sedimentation path is fully defined by its slope  $s$ , the intercept  $a$ , and its direction, which is given by the sign of the buoyant masses. For positive (negative) buoyant mass  $m_i$ ,

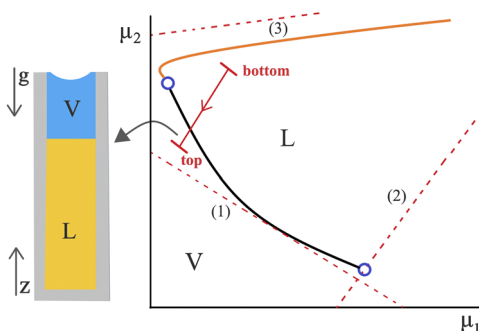


**FIG. 3.** Schematic bulk phase diagram of a colloidal binary mixture in the plane of chemical potentials  $\mu_1 - \mu_2$  at fixed temperature. The black solid line represents a binodal at which phases  $L$  and  $V$  coexist. The binodal ends at two critical points (empty circles). A percolation line (orange solid line) hits the binodal near a critical point. The red solid line represents the sedimentation path of a mixture in a sample of height  $h$  under gravity. The arrow indicates the direction of the path from the bottom to the top of the sample. The corresponding stacking sequence is bottom  $L$  and top  $V$ , as shown in the sketch. The red dashed lines are selected sedimentation paths for the limit of an infinite height sample: (1) a path tangent to the binodal, (2) a path that crosses an end point of a binodal, and (3) a path parallel to the asymptotic percolation line in the limit of infinite chemical potentials.

the local chemical potential  $\mu_i(z)$  decreases (increases) from the bottom to the top of the sample. Finite sedimentation paths<sup>25</sup> can also be considered, e.g., to study the effect of sample height and to make a direct comparison with experiments.

Both the intercept  $a$  and the slope  $s$  of the path are related to physical parameters of the system. The buoyant mass of species  $i$  is  $m_i = (\rho_{m,i} - \rho_s)v_i$ , where  $\rho_s$  is the solvent density,  $\rho_{m,i}$  is the mass density of species  $i$ , and  $v_i$  is the volume of a particle of species  $i$ . Hence, for a binary mixture in which both species are of the same material, the slope  $s$  is simply given by

$$s = \frac{m_2}{m_1} = \frac{v_2}{v_1} = \frac{\sigma_B^3}{\sigma_A^3} = \sigma^{*3}. \quad (21)$$

The intercept  $a$  fixes the location of the path in the plane of chemical potentials, and it is given by the slope  $s$  and the bulk chemical potentials of the sample in the absence of gravity. Hence, the composition and the concentration of the mixture affect the location of the path.

By changing the parameters  $a$  and  $s$ , different stacking sequences can appear. The sequences can be classified in a stacking diagram in the plane of slope  $s$  and intercept  $a$  of the sedimentation path.<sup>17,21</sup> In this plane, each point represents a sedimentation path and therefore a stacking sequence. The boundaries between different stacking sequences in the stacking diagram are formed by special sedimentation paths for which an infinitesimal change in either  $s$  or  $a$  might lead to a change in the stacking sequence. In the limit of an infinite height sample, there are three different types of boundaries in the stacking diagram. In Fig. 3, we show schematically a bulk phase diagram, a finite sedimentation path (finite sample height), and three examples of sedimentation paths that define boundaries between distinct stacking sequences in the stacking diagram. The three types of boundaries in the stacking diagram are as follows.

### 1. Sedimentation binodals

Formed by the set of all sedimentation paths that in bulk are tangent to a phase boundary [e.g., the path (1) in Fig. 3], such as binodal lines and percolation lines.

### 2. Terminal lines

Given by the set of sedimentation paths that cross an end point of a phase boundary [e.g., the path (2) in Fig. 3], such as a critical point or a percolation end point.

### 3. Asymptotic terminal lines

A bulk binodal or a percolation line in the plane of chemical potentials does not end at finite chemical potentials if it is either connected to a transition of one of the monocomponent systems or it represents a phase boundary that continues in the limit of infinite chemical potentials. In both cases, the set of sedimentation paths that are parallel to the asymptotic behavior of the phase boundary [e.g., line (3) of Fig. 3] correspond also to a boundary in the stacking diagram between different stacking sequences.

For samples of finite height, the sedimentation paths are not only determined by their slope and intercept, and hence, the stacking diagrams admit several representations.<sup>25</sup> Depending on the sample height, the possible stacking sequences are those given by the

stacking sequences of the infinite height limit plus their subsequences formed by removing stacks from either the top or the bottom of the sample.

### III. RESULTS

We begin by describing the phase behavior of mixtures with equal size particles in Sec. III A. In Sec. III B, we discuss the phase behavior of mixtures with particles of different sizes. Next, we focus on the effect of gravity in mixtures of particles with the same size in Sec. III C and with different sizes in Sec. III D. The phase diagrams are shown in reduced temperature,  $T^* = k_B T / \epsilon$ , and reduced osmotic pressure representations,  $P^* = p v_A / \epsilon$ , where  $v_A$  is the volume of particle 2A.

#### A. Phase behavior: Equal size particles

The bulk phase diagram for the mixture with equisized particles ( $\sigma_A = \sigma_B$ ) in the composition–temperature plane for a fixed osmotic pressure  $P^* = 7 \cdot 10^{-5}$  is shown in Fig. 4. Two fluid phases are stable: a low-density vapor phase,  $V$ , and a high-density liquid phase,  $L$ . It is informative to divide the vapor phase in  $V_1$  and  $V_2$ : the vapor phases rich in species 1 (2A) and 2 (3B), respectively. By doing so, the percolation lines are easily distinguishable and the abundance of each species relative to the other is specified. There are two coexistence regions, each one ending at a lower critical point. The maximum number of bonds is determined by the composition of both species. Particles 3B allow up to three bonds, but since we are considering interspecies bonds only, we need more 2A than 3B particles to allow a fully connected system. This is why the denser phase occurs at values around  $x = 0.6$ , where most bonds are realizable. The low temperature vapor phases occur when the mixture is made mostly of one of the species. The asymmetry in the coexistence regions is due to the different functionality of the particles.

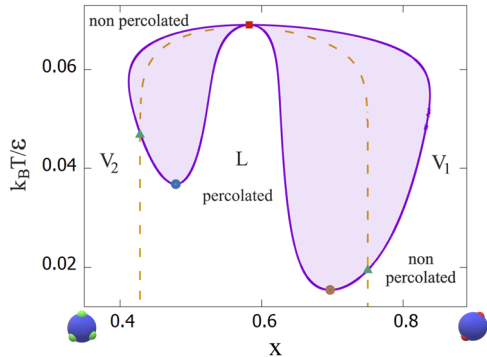


**FIG. 4.** Bulk phase diagram of the mixture with equal size particles in the composition–temperature plane for the reduced pressure  $P^* = p v_A / \epsilon = 7 \cdot 10^{-5}$ . The violet solid line is the binodal, which encloses the coexistence region. The brown circle denotes the critical point of the phase rich in 2A, and the blue circle denotes the critical point of the phase rich in 3B. The square is the azeotropic point. The orange dashed lines are the percolation lines that cross the coexistence regions at the points indicated by green triangles.  $V_1$  ( $V_2$ ) stands for the vapor phase rich in 2A (3B), and  $L$  stands for the liquid phase.

It is not possible to classify this mixture following the work of van Konynenburg *et al.*,<sup>41</sup> as none of the two pure fluids undergoes liquid–vapor (LV) condensation, i.e., the coexistence regions do not extend up to the pure fluid compositions at  $x = 0$  and  $x = 1$ . A negative azeotropic point is present at  $x \approx 0.58$ . The percolation lines indicate the percolation threshold. In the region between the lines, the system percolates. The liquid phase is always percolated (i.e., the liquid phase forms always a network fluid). Inside the coexistence regions and close to the critical points, the system phase separates into a percolated vapor phase and a percolated liquid phase. The percolation lines cross the coexistence region at the percolation end points. These points are important when the effect of gravity is considered. Moving upward from these points and inside the coexistence region, the system divides into a percolated liquid and non-percolated vapor. As the temperature is increased, the two percolation lines get closer and finally meet in the azeotropic point. In the low temperature limit, using the laws of mass action [Eq. (7)] and the percolation condition [Eq. (16)], the percolation lines tend to (with  $n_A = 2$ ) the following:

- (a) if  $X_A \rightarrow 0$ ,  $x \rightarrow \frac{n_B}{3n_B - 2}$ ; for the system under study,  $n_B = 3$ , and so  $x \rightarrow 3/7$ .
- (b) if  $X_B \rightarrow 0$ ,  $x \rightarrow \frac{n_B(n_B - 1)}{2 + n_B(n_B - 1)}$ ; for the system under study,  $n_B = 3$ , and so  $x \rightarrow 3/4$ .

Note that for  $n_B \geq 3$ , there will always be a region between  $x = 1/3$  and  $x = 1$  where the system is percolated at sufficiently low temperatures.

The typical values of the packing fractions at coexistence can be inferred from the phase diagram representation of Fig. 5, where the binodal is plotted in the plane of packing fractions  $\eta_1$  and  $\eta_2$  of the two species at fixed temperature  $T^* = 0.065$ . (The pressure–composition representation of the bulk diagram at the same temperature is shown in Fig. 10 to discuss the effects of gravity.) In Fig. 5, each point represents a thermodynamic

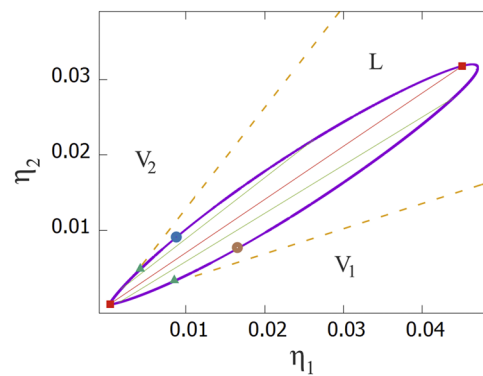


**FIG. 5.** Projection of the phase diagram at constant temperature ( $T^* = 0.065$ ) in the packing fraction representation. The violet solid line is the binodal line, the orange dashed lines the percolation lines that cross the coexistence regions at the points indicated by green triangles. The brown circle denotes the critical point of the phase rich in 2A, and the blue circle denotes the critical point of the phase rich in 3B. The thin red line is the tie line for the azeotropic point ( $P^* = 2.851 \cdot 10^{-5}$ ). The thin green lines are the tie lines for the pressure of  $P^* = 1 \cdot 10^{-4}$ .

state with (total) packing fraction  $\eta = \eta_1 + \eta_2$  and composition  $x = \eta_1/(\eta_1 + \eta_2)$ . There is no phase separation if  $\eta$  is larger than  $\sim 0.07$  (irrespective of composition). At lower densities, coexistence occurs at intermediate values of  $x$ . The three thin lines inside the two phase region are illustrative tie lines that connect coexisting points. At the azeotropic point, there is a single tie line (thin red line). In a range of pressures higher than that of the azeotropic point, there are two phase transitions (see, e.g., the two green tie lines obtained at  $P^* = 1 \cdot 10^{-4}$ ). The density of the coexisting liquid at each of the transitions differs significantly, and it is determined by the overall composition. For 2A rich systems (i.e.,  $x > 1/2$  or  $\eta_1 > \eta_2$ ), the coexisting liquid phase has a density that is significantly larger than the density of the coexisting liquid obtained at the same pressure for 3B rich systems. Note that one expects to obtain a qualitatively similar  $\eta_1 - \eta_2$  phase diagram for all the other temperatures where coexistence takes place and percolation is possible. Given that the tie lines represented in Fig. 5 correspond to reduced pressures of the same order of magnitude ( $10^{-5}, 10^{-4}$ ) of the binodals of Figs. 4, 6, and 8, it is expected that the packing fractions at which phase separation occurs will also have the same order of magnitude (i.e.,  $\eta_1$  and  $\eta_2 \approx 10^{-2}, 10^{-1}$ ).

We show the bulk phase diagrams in the composition–temperature plane for different values of the osmotic pressure in Fig. 6. The two phase regions shrink when the pressure is increased. Hence, higher pressure increases the tendency to mix. Increasing the pressure leads to a density increase [see Eq. (11)], which explains why the system is more prone to mix (if only homogeneous phases are considered). For pressures higher than  $P^* = 1.94 \cdot 10^{-4}$ , the 3B rich coexistence region disappears and there is only a closed miscibility gap with upper and lower critical points inside the percolated region. For pressures above  $P^* = 3.9 \cdot 10^{-4}$ , the LV condensation disappears and the system is completely miscible. The percolation line for the closed miscibility gap topology ( $P^* = 3.8 \cdot 10^{-4}$ ) is shown. The phase coexistence is completely inside the percolation line. Furthermore, as the

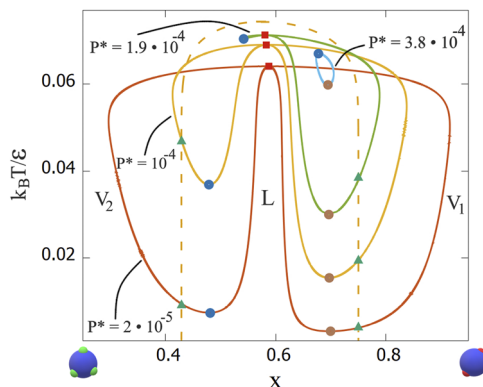


**FIG. 6.** Bulk phase diagrams in the composition–temperature plane for the reduced pressure  $P^* = 2 \cdot 10^{-5}$  (orange line),  $P^* = 10^{-4}$  (yellow line),  $P^* = 1.9 \cdot 10^{-4}$  (green line), and  $P^* = 3.8 \cdot 10^{-4}$  (blue line). The topology of the phase diagram changes for this last value. The blue circles are the critical points, and the red squares are the azeotropic points. The percolation lines are represented in yellow dashed lines, and they end in the green triangles (at the coexistence region).

percolation end points indicate, at lower temperatures, the percolation lines do not change.

In Fig. 7, we represent the critical properties of the mixture. In Fig. 7(a), the critical lines in the critical temperature vs critical packing fraction representation are shown. There is no empty liquid regime<sup>3</sup> since the critical densities do not tend to zero (if this were the case, it would be possible to have liquid phases at arbitrarily low densities). Nevertheless, the critical lines tend asymptotically to  $\eta_C^- \approx 0.0189$  in the phase rich in 3B and to  $\eta_C^+ \approx 0.0246$  in the phase rich in 2A, which are very low for liquid phases. In Fig. 7(b), critical pressure–critical temperature projections are represented. The critical line forms a closed loop starting and ending at  $P \rightarrow 0$  and  $T \rightarrow 0$ . In Fig. 7(c), we show the critical bonding probabilities,  $(1 - X_A)$  and  $(1 - X_B)$ . In the 2A rich phase, all 3B patches are bonded,  $(1 - X_B) \rightarrow 1$ , and the opposite happens for the 3B rich phase, i.e.,  $(1 - X_A) \rightarrow 1$ . In Fig. 7(d), the critical average size of the clusters  $\langle M \rangle$  is plotted [see Eq. (17)]. As  $T \rightarrow 0$ , the average size of the clusters in the 2A rich phase tends to  $\langle M \rangle^+ \rightarrow 10.9$  and in the 3B rich phase to  $\langle M \rangle^- \rightarrow 23.7$ . The phase rich in 3B has a larger average cluster size because these particles allow more bonds. As the critical temperature increases,  $\langle M \rangle^+$  and  $\langle M \rangle^-$  approach the same value.

## B. Phase behavior: Different size particles

Next, we study the effect of changing the relative size of the particles  $\sigma^* = \sigma_B/\sigma_A$ . Since in the experimental systems<sup>6,7,9,11</sup> the linkers are always smaller than the monomers, we restrict our analysis to the case  $\sigma^* \geq 1$ . An increase in  $\sigma^*$  corresponds to increasing the size

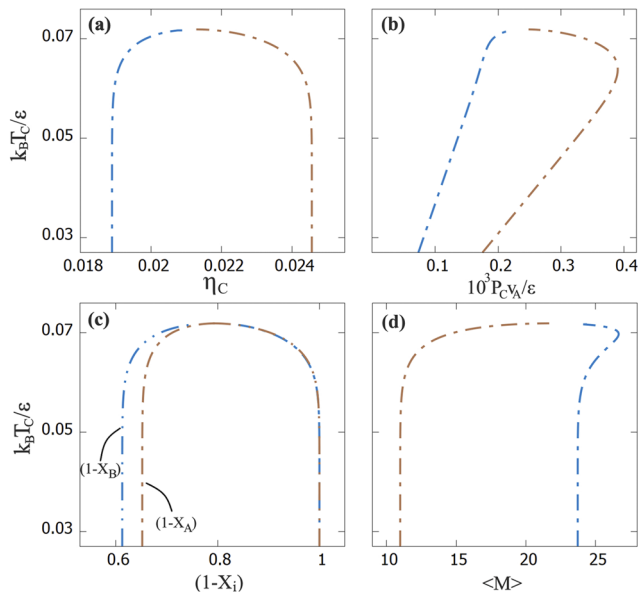


**FIG. 7.** Critical properties of the mixture with equal size particles. The critical lines corresponding to the phase rich in 2A are depicted in brown and in blue for the phase rich in 3B. (a) Critical temperature vs critical packing fraction. (b) Critical temperature vs critical pressure. (c) Critical temperature vs critical bonding probabilities. (d) Critical temperature vs critical average size of the clusters.

of the 3B particles, with the size of the 2A particles fixed. We plot in Fig. 8 the phase diagrams for mixtures with particles of different sizes at a fixed pressure of  $P^* = 7 \cdot 10^{-5}$ .

The phase diagrams have the same topologies as for mixtures with equal size particles: as  $\sigma^*$  increases, the coexistence regions get smaller, similar to the effect of increasing the pressure for the case of mixtures with equal size particles. Above  $\sigma^* = 1.63$ , the 3B rich phase disappears and the topology of the phase diagram changes to a single closed miscibility gap. Above  $\sigma^* = 1.95$ , the gap disappears and the system becomes completely miscible at all temperatures. By increasing the size of the 3B particles, we increase the interspecies excluded volume and the particles have less volume to explore, making it harder to bond and causing the miscibility gaps to shrink. The calculation of the binodal near the critical region is incomplete. This is due to numerical problems caused by the difficulty in minimizing the functional  $g(x)$ , Eq. (11), near the critical region. Nevertheless, we do not expect this region to change considerably. The percolation lines show that the liquid phase is always percolated. The position of the percolation lines changes only slightly by changing the size. This is because the size dependence in the eigenvalues is in the probabilities  $(1 - X_i)$ , and as it is shown below [see Fig. 9(c)], the effect of changing the size makes  $(1 - X_A)$  increase and  $(1 - X_B)$  decrease, which compensate almost exactly, causing the value of  $\lambda_+$ , Eq. (16), to change very little. The asymptotic behavior of the percolation lines at low temperature does not change by changing  $\sigma^*$  (similar to what happened by increasing the pressure): It tends to  $x \rightarrow 3/7$  in the phase rich in 3B and to  $x \rightarrow 3/4$  in the phase rich in 2A. Inside the coexistence regions, the percolation lines continue and meet in the azeotropic point. For the closed miscibility gap, in contrast to the previous case, the gap is not completely inside the percolated region. Instead, the percolation line crosses the coexistence region.

The critical properties of the mixtures are shown in Fig. 9. As we increase the size of the 3B particles, the critical packing fractions of the mixture tend to higher values [see Fig. 9(a)], which is not

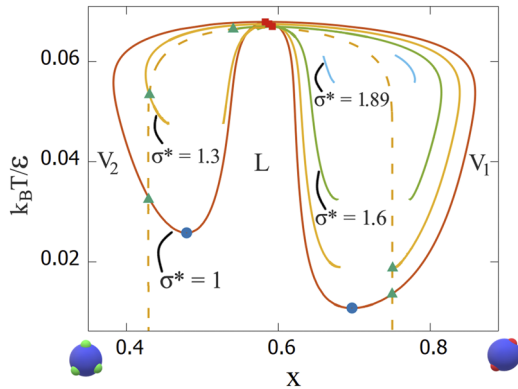


**FIG. 8.** Phase diagrams in the temperature–composition plane for  $P^* = 7 \cdot 10^{-5}$  and different size mixtures. The values of  $\sigma^* = \sigma_B/\sigma_A$  are  $\sigma^* = 1$  (orange line),  $\sigma^* = 1.3$  (yellow line),  $\sigma^* = 1.6$  (green line), and  $\sigma^* = 1.89$  (blue line). The percolation lines are plotted as dashed lines. The triangles indicate the points where the percolation line hits the binodal, the circles indicate the critical points, and the squares indicate the azeotropic point. The open binodals are due to numerical problems (see the text).

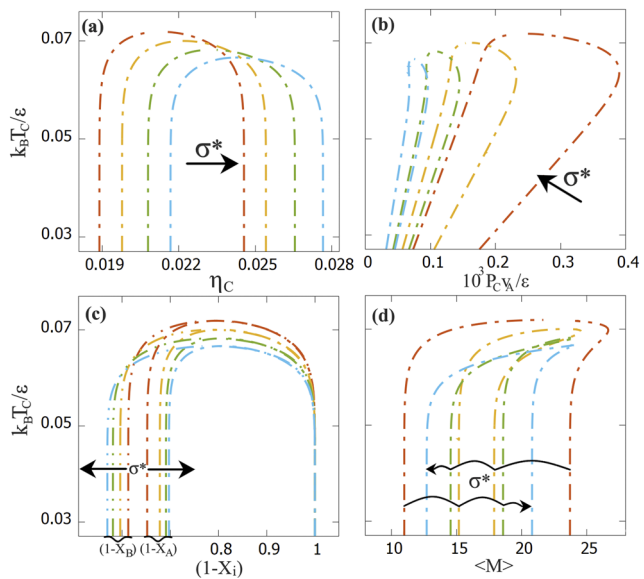


**FIG. 9.** Critical properties for mixtures of different size particles. The color scheme is the following:  $\sigma^* = \sigma_B/\sigma_A = 1$  (orange line),  $\sigma^* = 1.3$  (yellow line),  $\sigma^* = 1.6$  (green line), and  $\sigma^* = 1.89$  (blue line). The arrows represent the direction of increasing  $\sigma^*$ . (a) Critical temperature vs critical packing fraction. (b) Critical temperature vs critical pressure. (c) Critical temperature vs critical bonding probabilities. (d) Critical temperature vs critical average size of the clusters.

surprising since the system is denser. For the pressure–temperature projections in Fig. 9(b), the closed loops get smaller with increasing size, which is an indication that the coexistence regions shrink. There is also a shift of the closed loops to lower critical temperatures and pressures as the size of the 3B particles increases. In Fig. 9(c), the critical bonding probabilities are represented by  $(1 - X_A)$  and  $(1 - X_B)$ . As  $\sigma^*$  increases, it becomes harder to find a bonded 3B patch in the rich 3B phase (2A patches are completely bonded) and it becomes easier to find a bonded 2A patch in the rich 2A phase (3B patches are completely bonded). This describes the effect of changing the size of the particles. The behavior of the average cluster size is the most interesting, Fig. 9(d). The clusters in the 3B rich phase tend to smaller values as  $\sigma^*$  is increased (the probability of bonding 3B particles decreases). In the 2A rich phase, the average size of the clusters increases (the probability of bonding 2A particles increases). For size ratios larger than  $\sigma^* \approx 1.5$ , the clusters in the 2A rich phase become larger than those in the 3B rich phase. In recent works,<sup>42,43</sup> linker-particle binary mixtures (with  $n_B = 6$ ) where the linker is a polymer have been studied using theories similar to those considered here. In particular, the effects of polymer stiffness<sup>42</sup> and length<sup>43</sup> have been investigated and represented (Fig. 2 of Ref. 42 and Fig. 3 of Ref. 43) in an (inverse) temperature vs  $\eta_2$  phase diagram at fixed composition ( $x = 0.6$ , in our notation). It is reported that coexistence is obtained below a certain temperature ( $k_B T/\epsilon \approx 0.06\text{--}0.07$ ), which barely changes with stiffness<sup>42</sup> or length.<sup>43</sup> Figure 8 shows that a similar behavior is expected from our theory: At a fixed intermediate composition close to that of the azeotropic point ( $x \approx 0.6$ ), one would always obtain critical temperatures close to  $k_B T_c/\epsilon \approx 0.06\text{--}0.07$ , irrespective of the size ratio  $\sigma^*$ .

### C. Sedimentation: Equal size particles

We proceed to study sedimentation–diffusion–equilibrium in the infinite height sample approximation. As in standard experimental conditions, we work at constant temperature. Figure 10 shows the bulk phase diagram of a mixture of equal size particles in the pressure–composition and also in the plane of chemical potentials. The pressure–composition diagrams are obtained in a similar way as the temperature–composition diagrams, but keeping the temperature constant instead of the pressure. The chemical potentials are calculated considering that the Gibbs free energy per particle is simply  $g = x\mu_1 + (1-x)\mu_2$ . Hence,  $\mu_1$  and  $\mu_2$  can be obtained from the value of the tangent to  $g(x)$  at  $x=1$  and  $x=0$ , respectively.

The diagrams shown in Fig. 10 are representative of the system under study as they show the two topologies already discussed. In Figs. 10(a) and 10(b), a closed miscibility gap with upper and lower critical points is illustrated. For the values of the pressure plotted, the system is always percolated. At temperatures below  $T^* = 0.071$ , a second coexistence region appears, Figs. 10(c) and 10(d). The bulk phase diagram exhibits a positive azeotropic point and two upper critical points. We also represent the percolation lines. The system percolates in the region enclosed by the percolation lines. At higher temperatures, the phase separation region shrinks and eventually disappears, similarly to the effect of increasing the pressure (Fig. 6). In addition, since the percolation lines intercept the binodal from the vapor phase [see Fig. 10(d)], it is possible to find a low density vapor

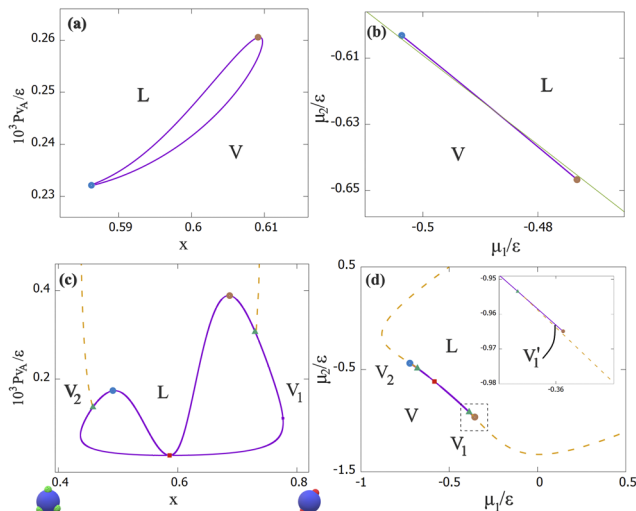


**FIG. 10.** Pressure–composition bulk diagrams at constant temperature [(a) and (c)] and corresponding diagrams in the plane of chemical potentials [(b) and (d)]. The temperature is set to [(a) and (b)]  $T^* = 0.0718$  and [(c) and (d)]  $T^* = 0.065$ . The violet lines indicate the binodals, and the yellow dashed lines indicate the percolation lines {not shown in [(a) and (b)] as the system is always percolated} that intercept the binodal at the points marked by triangles. The blue circles indicate the critical points of the 3B rich phase, and the brown circles indicate the critical points of the 2A rich phase. The azeotropic point is marked by the red square. The green line in (b) is an example of a sedimentation path corresponding to the stacking sequence LV from bottom to top (see Fig. 11 for the point corresponding to this sedimentation path).

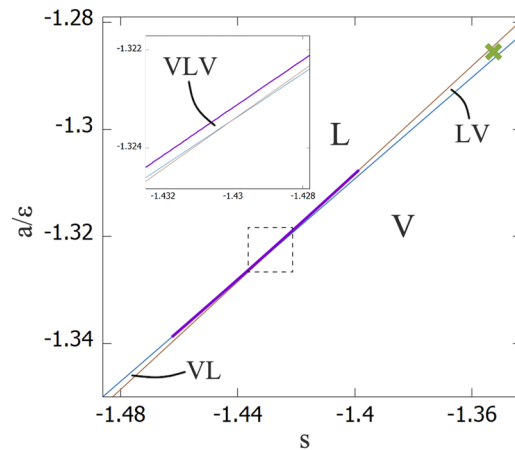


**FIG. 11.** Stacking diagram of a mixture of equal size particles at temperature  $T^* = 0.0718$ . The violet line is the sedimentation binodal. The blue and brown lines are the terminal lines of paths that cross bulk critical points. Each region defines a different stacking sequence, as indicated. The path corresponding to the green cross is represented in the bulk phase diagram, Fig. 10(b).

phase that is percolated. We define therefore  $V'_1$  and  $V'_2$  as the vapor percolated phases. This helps us to interpret the stacking sequences in the stacking diagram.

The stacking diagram in the presence of gravity is calculated using the phase diagrams in the plane of chemical potentials, as described in Sec. II C. In Fig. 11, we plot the stacking diagram for the case of the closed miscibility gap shown in Figs. 10(a) and 10(b), i.e.,  $T^* = 0.0718$ . The stacking diagram consists of a sedimentation binodal (formed by the paths tangent to the bulk binodal) and two terminal lines (formed by the paths that cross the critical points). These lines divide the stacking diagram in different

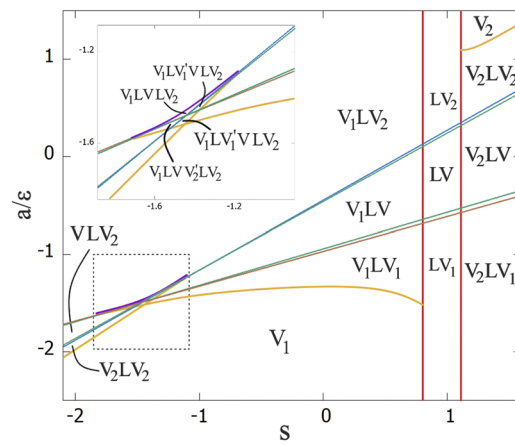


**FIG. 12.** Stacking diagram of a mixture of equal size particles at temperature  $T^* = 0.065$ . The violet line is the sedimentation binodal of the bulk binodal. The yellow lines correspond to the sedimentation binodals of the percolation lines. The blue and green lines are the terminal lines corresponding to the critical points and the percolation end points, respectively. The red vertical lines are the asymptotic terminal lines of the percolation lines.

regions that correspond to different stacking sequences. The stacking sequence of each region is found by selecting a point inside the region, plotting the corresponding sedimentation path in the bulk phase diagram, and then reading the sequence by looking at the bulk regions covered by the path. As an example, we highlight with a cross a point in the stacking diagram of Fig. 11 and show its corresponding sedimentation path in the bulk phase diagram of Fig. 10(b). The stacking sequences are named from the bottom to the top of the sample. Hence, the stacking sequence *LV* forms a liquid phase at the bottom of the sample and a vapor phase at the top (the opposite occurs for the stacking sequence *VL*). Although there are only two stable phases in the bulk, *L* and *V*, the stacking diagram contains five different stacking sequences. The stacking sequence *VLV* can be obtained for a very small range of slopes of the sedimentation paths for which the path crosses the bulk binodal twice.

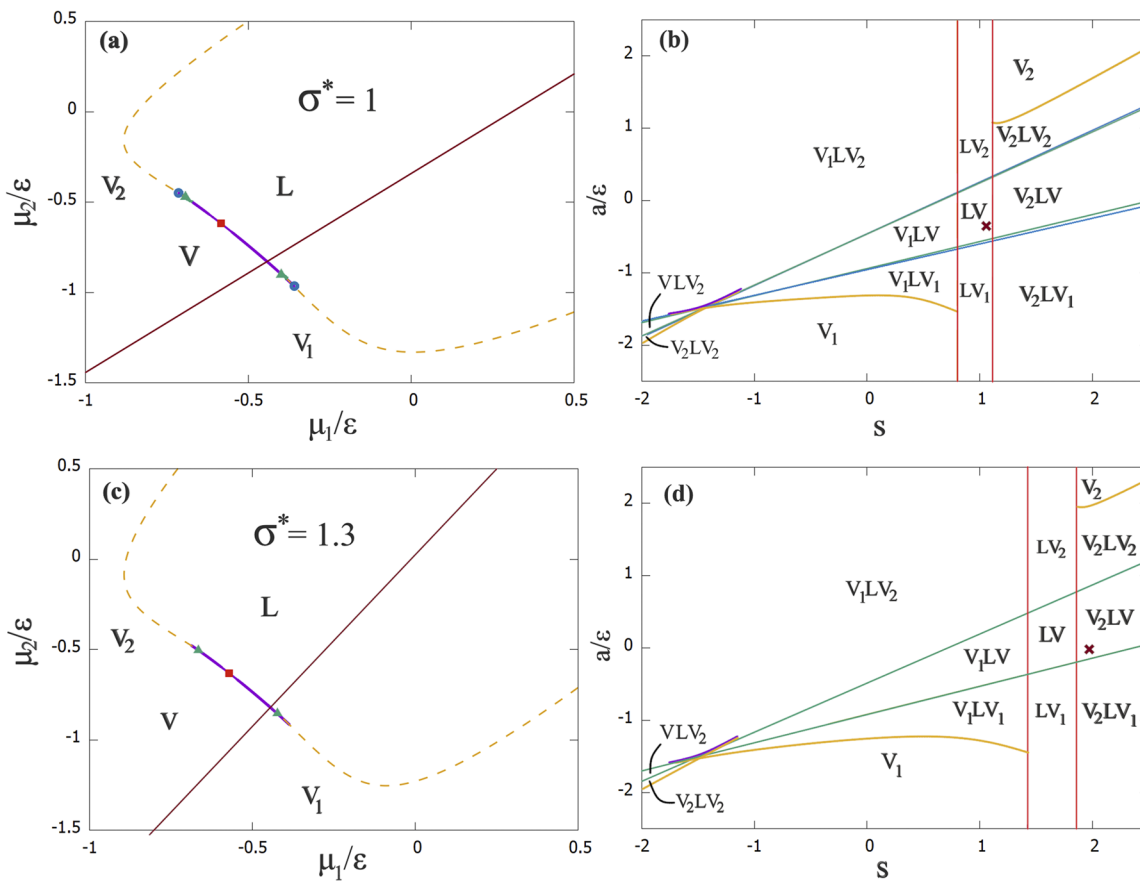
Next, we show in Fig. 12 the stacking diagram at  $T^* = 0.065$  for which the bulk diagram shows two coexistence regions. The stacking

diagram consists of three sedimentation binodals (one corresponding to the bulk binodal and two others to the percolation lines), four terminal lines (two for the critical points and two for the percolation end points), and two asymptotic terminal lines corresponding to the asymptotic behavior of the percolation lines at very high chemical potentials. We obtain over 20 different stacking sequences. Some of the stacking sequences are only possible for a small range of parameters  $a$  and  $s$  (see the inset of Fig. 12).

#### D. Sedimentation: Different size particles

We have shown in Sec. III B that the phase diagrams obtained for mixtures with particles of different sizes have the same topologies as those for equal size particles. Hence, the stacking diagrams of mixtures with particles of different sizes have also the same type and number of boundaries between different stacking sequences.

Here, we investigate if a stacking sequence can be altered by changing the size of the particles only. To this end, we compare



**FIG. 13.** Bulk phase diagrams (left) and corresponding stacking diagrams (right). The temperature is set at  $T^* = 0.065$ . Panels (a) and (c) show the bulk phase diagrams in the plane of chemical potentials of mixtures with relative sizes  $\sigma^* = \sigma_B/\sigma_A = 1$  and  $\sigma^* = 1.3$ , respectively. Panels (b) and (d) show the corresponding stacking diagrams in the plane of slope  $s$  and intercept  $a$  of the paths for  $\sigma^* = 1$  and  $\sigma^* = 1.3$ , respectively. One point in the stacking diagram represents a sedimentation path in the bulk phase diagram. Illustrative sedimentation paths with stacking sequences *LV* in the equal size system (a) and *VLV* in the different size system (c) are shown as red solid lines. These paths are highlighted with red crosses in the corresponding stacking diagrams [(b) and (d)]. Each region in the stacking diagram contains all paths that give rise to the indicated stacking sequence.

stacking diagrams of mixtures with equal and different size particles at the same temperature (corresponding to the phase diagrams with the same topology). We consider a sedimentation path for equal size particles (a point in the stacking diagram) and map it to a system with different size particles. Assuming that the particles are made of the same material, we transform the slope  $s$  in the equal size system to the slope  $s'$  in the different size system according to Eq. (21), i.e.,

$$s' = (v'_2/v'_1)s = \sigma^{*3}s, \quad (22)$$

where  $v'_i$  is the particle volume species  $i$  in the different size system. The parameter  $a = \mu_2^b - s\mu_1^b$  is affected by this change and also by the change in the corresponding chemical potentials. We consider that both systems share the same bulk chemical potentials, i.e.,

$$\mu_i'^b = \mu_i^b, \quad i = 1, 2. \quad (23)$$

Hence, in the different size system, the path has an intercept given by  $a' = \mu_2'^b - s'\mu_1'^b$ .

In Fig. 13, we plot the bulk phase diagrams in the plane of chemical potentials and their corresponding stacking diagrams for systems with equal ( $\sigma^* = 1$ ) and different ( $\sigma^* = 1.3$ ) size particles. Although the stacking diagrams of both mixtures are similar, it is clearly possible to change the stacking sequences by simply altering the size of the particles (see the location of the highlighted paths in the stacking diagrams). The change is driven by the different value of the slope of the path, which is a direct consequence of the different particle sizes in both mixtures. In general, this change in the stacking sequence is possible for points in the stacking diagram, which are close to boundaries between different stacking sequences. Changes in the stacking sequence by altering the particle sizes also occur if the bulk diagrams of both mixtures differ substantially. As shown in Sec. III B, the topology of the bulk phase diagram (and hence that of the stacking diagram) changes if the size difference between the particles is large enough. For such cases, there are stacking sequences in one system, which simply do not occur in the other system.

#### IV. CONCLUSIONS

The phase behavior of linker-particle aggregating systems has been investigated using a binary mixture of patchy particles in which one species has two patches of type A and the other has three patches of type B. Only interspecies bonding (AB bonds) is allowed. The fraction of bonds can be controlled by the energy scale of the bonds AB and by the composition of the mixture. The temperature-composition and the pressure-composition phase diagrams were shown to exhibit two topologies: At low temperatures (or high bonding energies) and low pressures, there are two coexistence regions (one rich in 2A particles and another in 3B) with lower critical points and an azeotropic point. At intermediate temperatures and pressures, there is a single miscibility gap with upper and lower critical points. The liquid phase at intermediate compositions is always percolated, and at low temperatures and pressures, it is possible to obtain a percolated vapor in a narrow region of the phase diagram. The analysis of the critical properties has shown

that the empty fluid regime<sup>3,14</sup> is never reached and that the phase rich in 3B particles forms larger clusters than the phase rich in 2A. The analysis of mixtures with particles of different sizes has shown that increasing the size  $\sigma_B$  of 3B particles relatively to the size  $\sigma_A$  of 2A linkers does not change the topologies of the phase diagrams but mimics the effect of increasing the temperature or the pressure shrinking the region of phase coexistence. The percolation lines are mostly unaffected by the change in particle sizes. These results suggest that the size of the particles can be used as an extra variable to control aggregation, namely, to avoid phase separation and thus optimize the structure of equilibrium gels.

It is expected that gravitational effects become important when the linker-particle aggregating system is formed by colloidal particles. The stacking diagrams are richer than the bulk phase diagrams. The bulk diagrams with a single miscibility gap originate five possible stacking sequences. The bulk diagrams with two coexistence regions originate more than 20 different stacking sequences under gravity (some of them containing six layers). It is possible to alter the stacking sequence by changing the relative size of the components of the mixture.

We have obtained results for the bulk phase diagrams that are in line with those of Ref. 8. In addition, we have calculated the phase diagrams in several representations and incorporated the effects of different particle sizes and that of gravity. From this analysis, we conclude that the size of the particles can be used to control the phase behavior of the mixture, to tune the extent of phase separation, and to control the stacking sequences displayed under gravity.

Finally, note that the theory developed in this work can be applied to any combinations of the parameters  $(n_A, n_B)$  and  $(\sigma_1, \sigma_2)$  and therefore can be used to explore the thermodynamics and structure of other binary mixtures where particles of different species bond strongly but in a limited number.

#### ACKNOWLEDGMENTS

R.B.T., J.M.T., and M.M.T.d.G. acknowledge financial support from the Portuguese Foundation for Science and Technology (FCT) under Contract Nos. UIDB/00618/2020 and UIDP/00618/2020. D.d.l.H. acknowledges support from the German Research Foundation (DFG) via Project No. 436306241. R.B.T. acknowledges support from the Erasmus+ programme of the European Union.

#### DATA AVAILABILITY

The data that support the findings of this study are available from the corresponding author upon reasonable request.

#### REFERENCES

- M. Kamp, B. de Nijs, M. N. van der Linden, I. de Feijter, M. J. Lefferts, A. Alois, J. Griffiths, J. J. Baumberg, I. K. Voets, and A. van Blaaderen, *Langmuir* **36**, 2403 (2020).
- V. N. Manoharan, *Science* **349**, 1253751 (2015).
- E. Bianchi, J. Largo, P. Tartaglia, E. Zaccarelli, and F. Sciortino, *Phys. Rev. Lett.* **97**, 168301 (2006).
- J. Russo, J. M. Tavares, P. I. C. Teixeira, M. M. Telo da Gama, and F. Sciortino, *Phys. Rev. Lett.* **106**, 085703 (2011).
- L. Rovigatti, J. M. Tavares, and F. Sciortino, *Phys. Rev. Lett.* **111**, 168302 (2013).

- <sup>6</sup>A. L. Hiddessen, S. D. Rodgers, D. A. Weitz, and D. A. Hammer, *Langmuir* **16**, 9744 (2000).
- <sup>7</sup>V. T. Milam, A. L. Hiddessen, J. C. Crocker, D. J. Graves, and D. A. Hammer, *Langmuir* **19**, 10317 (2003).
- <sup>8</sup>B. A. Lindquist, R. B. Jadrich, D. J. Milliron, and T. M. Truskett, *J. Chem. Phys.* **145**, 074906 (2016).
- <sup>9</sup>Z. M. Sherman, A. M. Green, M. P. Howard, E. V. Anslyn, T. M. Truskett, and D. J. Milliron, *Acc. Chem. Res.* **54**, 798 (2021).
- <sup>10</sup>I. D. Stoev, T. Cao, A. Caciagli, J. Yu, C. Ness, R. Liu, R. Ghosh, T. O'Neill, D. Liu, and E. Eiser, *Soft Matter* **16**, 990 (2020).
- <sup>11</sup>N. Ghofraniha, P. Andreozzi, J. Russo, C. La Mesa, and F. Sciortino, *J. Phys. Chem. B* **113**, 6775 (2009).
- <sup>12</sup>G. C. Antunes, C. S. Dias, M. M. Telo da Gama, and N. A. M. Araújo, *Soft Matter* **15**, 3712 (2019).
- <sup>13</sup>D. de las Heras, J. M. Tavares, and M. M. Telo da Gama, *J. Chem. Phys.* **134**, 104904 (2011).
- <sup>14</sup>D. de las Heras, J. M. Tavares, and M. M. Telo da Gama, *Soft Matter* **7**, 5615 (2011).
- <sup>15</sup>R. Piazza, *Rep. Prog. Phys.* **77**, 056602 (2014).
- <sup>16</sup>H. H. Wensink and H. N. W. Lekkerkerker, *Europhys. Lett.* **66**, 125 (2004).
- <sup>17</sup>D. de las Heras and M. Schmidt, *Soft Matter* **9**, 8636 (2013).
- <sup>18</sup>F. M. van der Kooij and H. N. W. Lekkerkerker, *Phys. Rev. Lett.* **84**, 781 (2000).
- <sup>19</sup>L. Luan, W. Li, S. Liu, and D. Sun, *Langmuir* **25**, 6349 (2009).
- <sup>20</sup>D. de las Heras, N. Doshi, T. Cosgrove, J. Phipps, D. I. Gittins, J. S. van Duijneveldt, and M. Schmidt, *Sci. Rep.* **2**, 789 (2012).
- <sup>21</sup>D. de las Heras and M. Schmidt, *J. Phys.: Condens. Matter* **27**, 194115 (2015).
- <sup>22</sup>T. Drwenski, P. Hooijer, and R. van Roij, *Soft Matter* **12**, 5684 (2016).
- <sup>23</sup>G. Avvisati, T. Dasgupta, and M. Dijkstra, *ACS Nano* **11**, 7702 (2017).
- <sup>24</sup>D. de las Heras, L. L. Treffenstädt, and M. Schmidt, *Phys. Rev. E* **93**, 030601 (2016).
- <sup>25</sup>T. Geigeneifend and D. de las Heras, *J. Phys.: Condens. Matter* **29**, 064006 (2016).
- <sup>26</sup>P. I. C. Teixeira and J. M. Tavares, *Curr. Opin. Colloid Interface Sci.* **30**, 16 (2017).
- <sup>27</sup>W. Bol, *Mol. Phys.* **45**, 605 (1982).
- <sup>28</sup>N. Kern and D. Frenkel, *J. Chem. Phys.* **118**, 9882 (2003).
- <sup>29</sup>F. Sciortino, E. Bianchi, J. F. Douglas, and P. Tartaglia, *J. Chem. Phys.* **126**, 194903 (2007).
- <sup>30</sup>M. S. Wertheim, *J. Stat. Phys.* **35**, 35 (1984).
- <sup>31</sup>A. Santos, S. B. Yuste, and M. López de Haro, *J. Chem. Phys.* **117**, 5785 (2002).
- <sup>32</sup>N. F. Carnahan and K. E. Starling, *J. Chem. Phys.* **51**, 635 (1969).
- <sup>33</sup>M. S. Wertheim, *J. Stat. Phys.* **42**, 477–492 (1986).
- <sup>34</sup>W. G. Chapman, G. Jackson, and K. E. Gubbins, *Mol. Phys.* **65**, 1057 (1988).
- <sup>35</sup>L. Rovigatti, D. de las Heras, J. M. Tavares, M. M. Telo da Gama, and F. Sciortino, *J. Chem. Phys.* **138**, 164904 (2013).
- <sup>36</sup>M. Doi, *Soft Matter Physics* (Oxford University Press, 2013).
- <sup>37</sup>J. S. Rowlinson and F. L. Swinton, *Liquids and Liquid Mixtures*, 3rd ed. (Butterworth-Heinemann, 1982), pp. 86–131.
- <sup>38</sup>P. J. Flory, *J. Am. Chem. Soc.* **63**, 3083 (1941).
- <sup>39</sup>W. H. Stockmayer, *J. Chem. Phys.* **11**, 45 (1943).
- <sup>40</sup>J. M. Tavares, P. I. C. Teixeira, and M. M. Telo da Gama, *Phys. Rev. E* **81**, 010501 (2010).
- <sup>41</sup>P. H. van Konynenburg and R. L. Scott, *Philos. Trans. R. Soc. London, Ser. A* **298**, 495 (1980).
- <sup>42</sup>M. P. Howard, Z. M. Sherman, A. N. Sreenivasan, S. A. Valenzuela, E. V. Anslyn, D. J. Milliron, and T. M. Truskett, *J. Chem. Phys.* **154**, 074901 (2021).
- <sup>43</sup>M. P. Howard, R. B. Jadrich, B. A. Lindquist, F. Khabaz, R. T. Bonnecaze, D. J. Milliron, and T. M. Truskett, *J. Chem. Phys.* **151**, 124901 (2019).